

Electronic Supplementary Information (ESI) for
**Modulating the deep-level defects and charge extraction for
efficient perovskite solar cells with high fill factor over 86%**

Xingcheng Li,^{‡a} Xin Wu,^{‡b} Bo Li,^{‡b} Zeyan Cen,^a Yanbo Shang,^a Weitao Lian,^a Rui Cao,^a Lingbo Jia,^a Zhen Li,^b Danpeng Gao,^b Xiaofen Jiang,^a Tao Chen,^a Yalin Lu,^a Zonglong Zhu^{*bc} and Shangfeng Yang^{*a}

^{a.} *CAS Key Laboratory of Materials for Energy Conversion, Anhui Laboratory of Advanced Photon Science and Technology, Department of Materials Science and Engineering, University of Science and Technology of China, Hefei 230026, China. Email: sfyang@ustc.edu.cn*

^{b.} *Department of Chemistry, City University of Hong Kong, Kowloon, Hong Kong, China. Email: zonglzhu@cityu.edu.hk*

^{c.} *Hong Kong Institute for Clean Energy, City University of Hong Kong, Kowloon 999077, Hong Kong, China*

[‡] These authors contributed equally.

Contents

S1. Incorporation and uniformity of Cs and Br elements within CsPbBr₃-incorporated FAPbI₃ perovskite film.	3
S2. Statistics of device performance.	6
S3. Comparison of FF and PCE obtained in this work with those reported in literatures.	13
S4. Stability data.	15
S5. XRD patterns of FAPbI₃ films with different amounts of CsPbBr₃.	17
S6. Geometric illustration of the crystal structure and radially integrated curves extracted from GIXRD patterns.	20
S7. SEM images of FAPbI₃ and 1.0 mol% CsPbBr₃-FAPbI₃ perovskite films.	21
S8. TAS at different delay times.	23
S9. UV-vis spectra and the plots of $(\alpha h\nu)^2$ vs energy ($h\nu$) of the control and target perovskite films.	24
S10. Enlarged DLTS spectra and Arrhenius plot.	25
S11. SCLC analysis.	27
S12. EIS analysis.	29
S13. Dark $J-V$ curves of the control and target devices.	31
S14. FF loss analysis.	31
References	34

S1. Incorporation and uniformity of Cs and Br elements within CsPbBr₃-incorporated FAPbI₃ perovskite film.

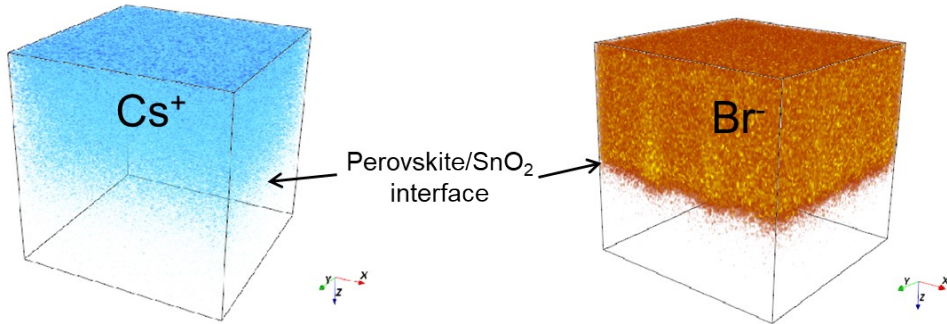


Fig. S1 Time-of-flight secondary ion mass spectrometry of Cs⁺ and Br⁻ results of FTO/SnO₂/KCl/1.0 mol% CsPbBr₃-FAPbI₃ perovskite (target).

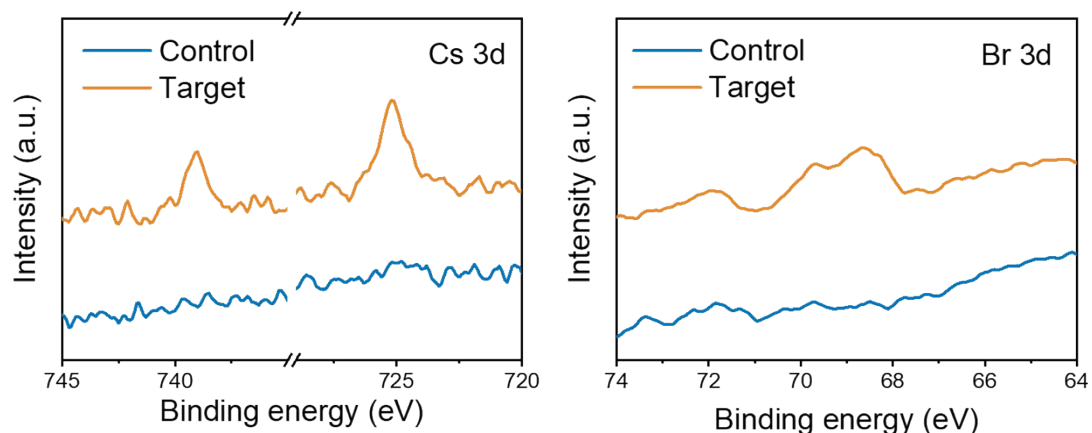


Fig. S2 X-ray photoelectron spectroscopy (XPS) of the control and target perovskite films.

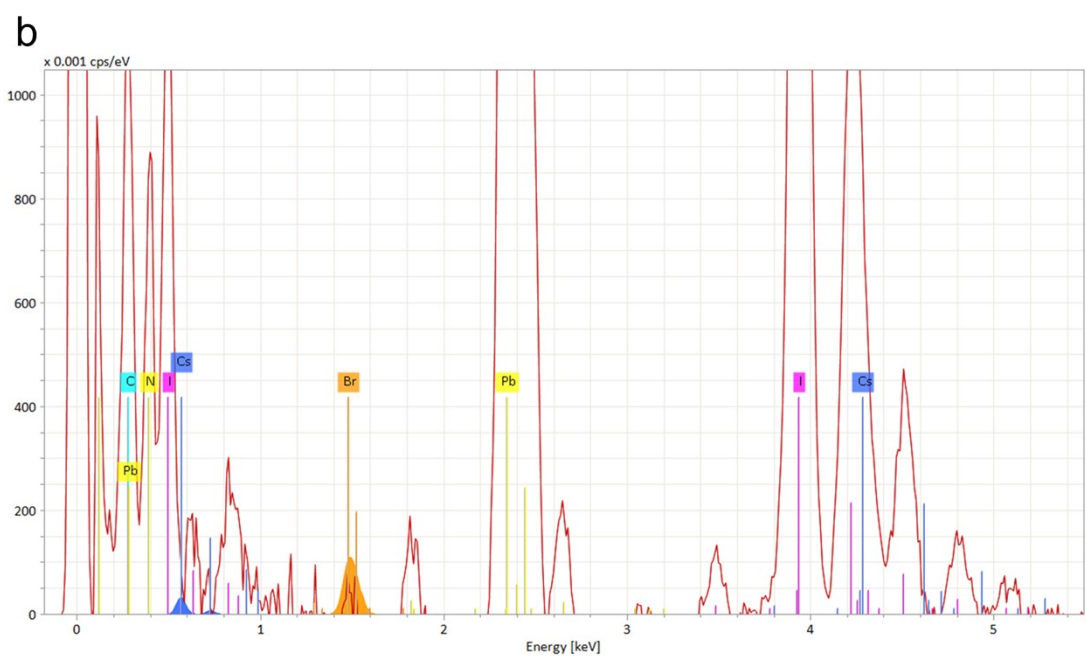
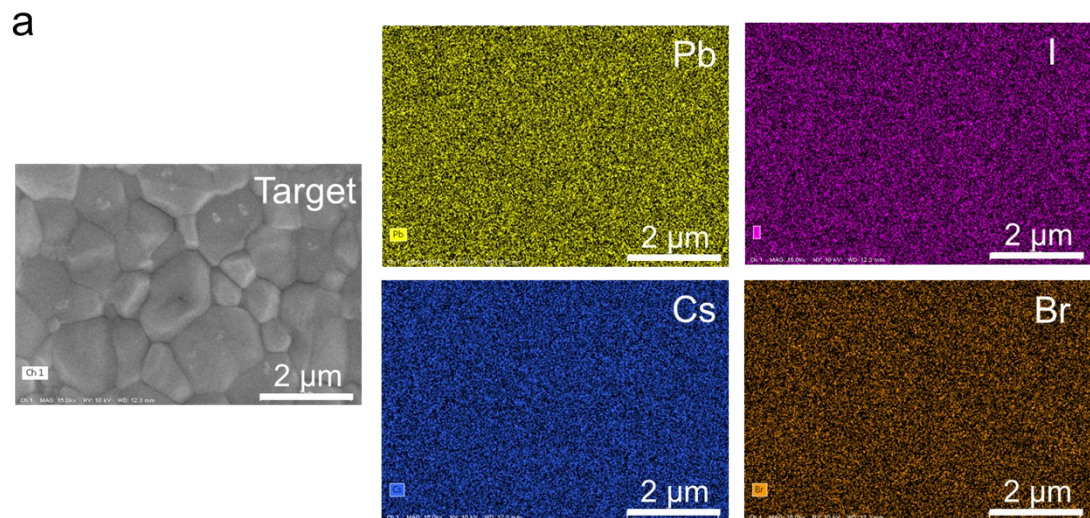


Fig. S3 The top-view SEM image and energy dispersive X-ray (EDX) mapping of the 1.0 mol% CsPbBr₃-FAPbI₃ (target) perovskite film.

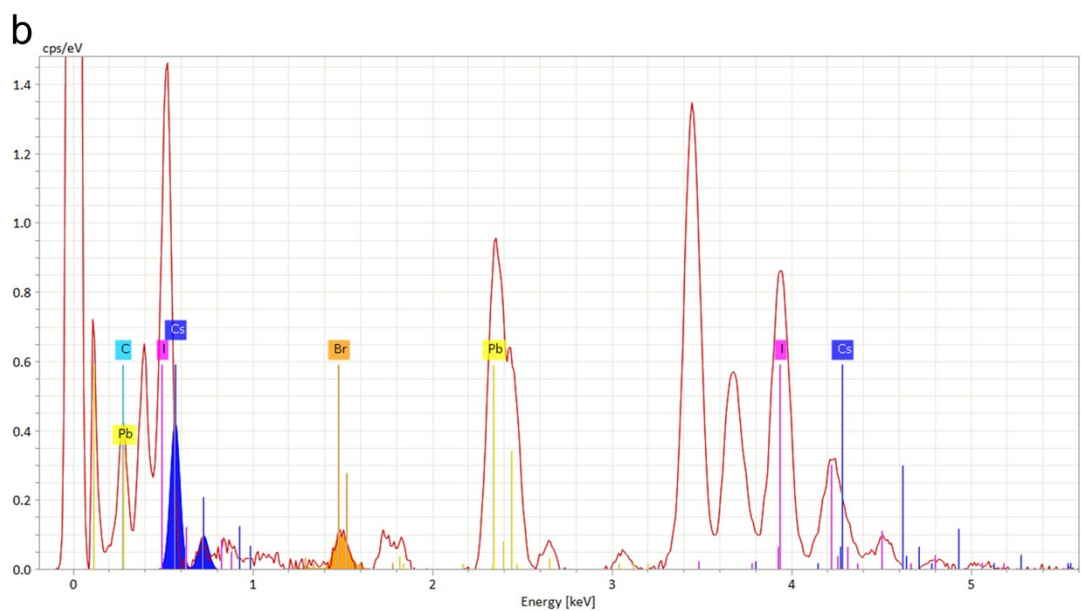
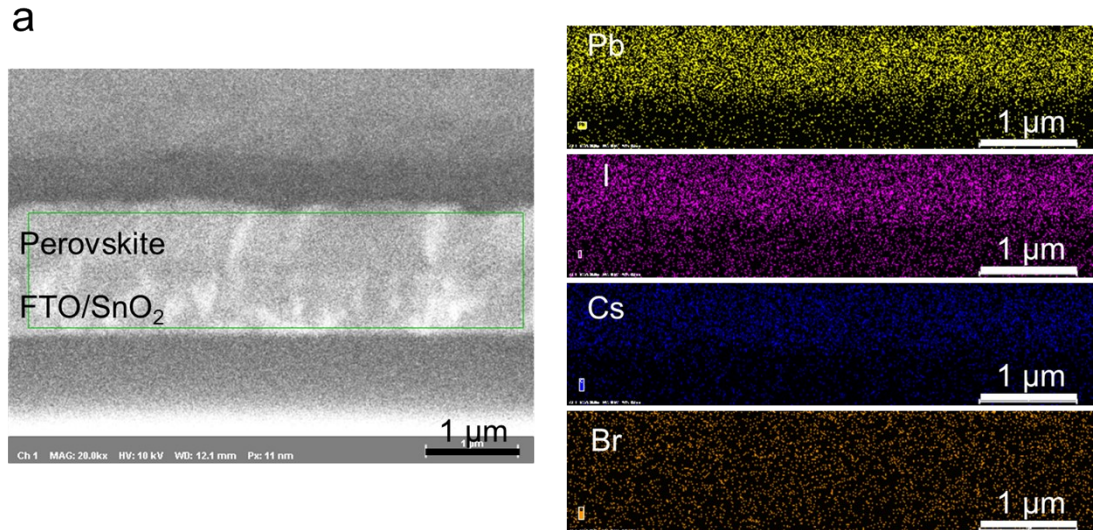


Fig. S4 The cross-sectional SEM image and energy dispersive X-ray (EDX) mapping of the 1.0 mol% CsPbBr₃-FAPbI₃ (target) perovskite film.

S2. Statistics of device performance.

Table S1 Photovoltaic parameters of perovskite solar cells fabricated with different amounts of CsPbBr₃ measured under one sun illumination (AM 1.5G, 100 mA cm⁻²).

Molar ratio ^a	V_{OC}^b (V)	J_{SC}^b (mA cm ⁻²)	FF ^b (%)	PCE ^b (%)
0%	1.089±0.009	25.63±0.15	82.59±0.72	23.05±0.21
0.5%	1.111±0.006	25.52±0.24	85.41±0.38	24.21±0.26
1.0%	1.131±0.008	25.46±0.17	85.78±0.40	24.71±0.19
2.0%	1.136±0.007	25.39±0.22	84.92±0.80	24.49±0.25

^a The molar ratio of CsPbBr₃ relative to PbI₂ in the perovskite precursor solution.

^b Averaged 30 devices fabricated independently.

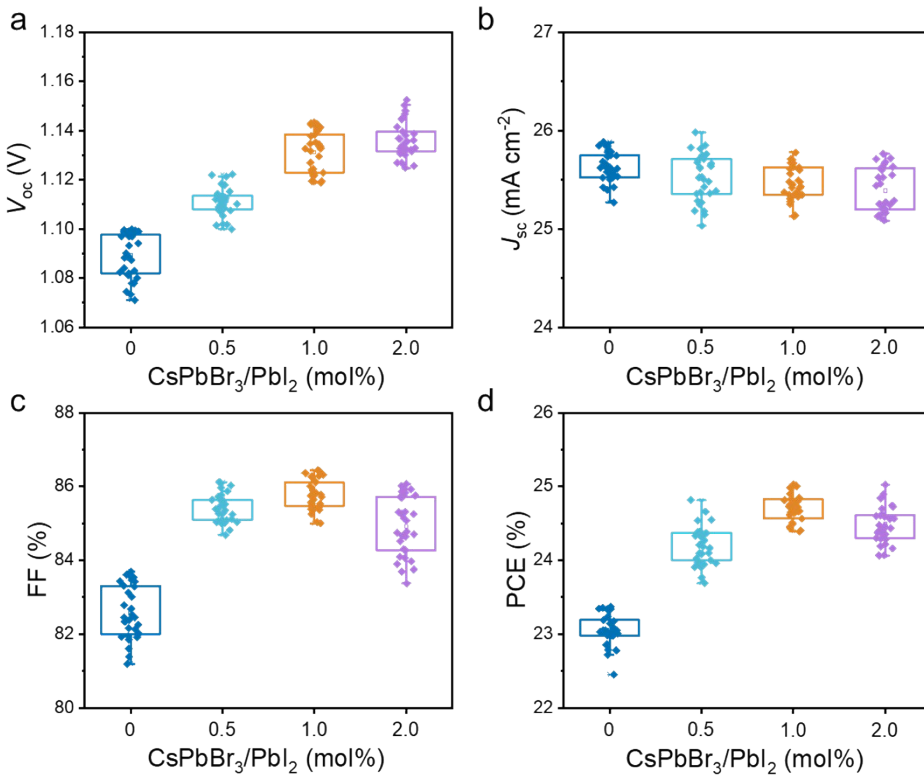


Fig. S5 Device statistics for V_{OC} **a**, J_{SC} **b**, and FF **c** and PCE **d** for the devices with different amounts of CsPbBr₃.

Table S2 Photovoltaic parameters of the devices without and with pre-crystallized CsPbBr₃ and PbBr₂/CsBr powder, respectively.

Additive	V_{OC}^a (V)	J_{SC}^a (mA cm ⁻²)	FF ^a (%)	PCE ^a (%)
w/o	1.074±0.011	25.60±0.28	83.73±0.96	23.02±0.29
1.0 mol% CsPbBr ₃	1.129±0.004	25.54±0.13	85.60±0.60	24.69±0.11
1.0 mol% PbBr ₂ ^b +CsBr	1.107±0.007	25.57±0.24	84.19±0.98	23.83±0.31
1.0 mol% PbBr ₂ ^c +CsBr	1.121±0.005	25.56±0.25	84.76±0.84	24.28±0.29

^a Averaged 10 devices fabricated independently.

^b The same to the PbBr₂ used to synthesize CsPbBr₃ crystal.

^c High purity PbBr₂ (Alfa Aesar, 99.999%).



170017163974



中国认可
国际互认
检测
TESTING
CNAS L8490

Test and Calibration Center of New Energy Device and Module,
Shanghai Institute of Microsystem and Information Technology,
Chinese Academy of Sciences (SIMIT)
235, Chengbei Road, Jiading, Shanghai, China

Measurement Report

Client Name University of Science and Technology of China (USTC)

Client Address 96 Jinzhai Road, Hefei, Anhui Province, P.R.China

Sample Perovskite solar cell

Manufacturer USTC, Shangfeng Yang Group

Application SIMITL72021102501

Measurement Date 25th October, 2021

Performed by:

Qiang Shi
Qiang Shi



Reviewed by:

Yating Zhang
Yating Zhang

Approved by:

Zhengxin Liu
Zhengxin Liu

Date: Oct. 25. 2021

The measurement report without signature and seal are not valid. This report shall not be reproduced, except in full, without the approval of SIMIT.

Sample Information

Sample Type	Perovskite solar cell
Quantity	1
Serial No.	39-2#
Measurement Item	I-V characteristic
Measurement Environment	23.9±2.0°C, 41.5±5.0%R.H

Measurement of I-V characteristic

Reference cell	PVM1124
Reference cell Type	mono-Si, WPVS, calibrated by NREL (ISO 2045)
Calibration Value/Date of Calibration for Reference cell	144.9mA/ Aug. 2021
Measurement Conditions	STC, linear sweep based on IEC 60904-1:2006
Measurement Equipment/ Date of Calibration	Steady State Solar Simulator (YSS-T155-2M) / May.2021 IV test system (ADCM 6246) / April. 2021 SR Measurement system (CEP-25ML-CAS) / April.2021
Mismatch Factor	SMM=0.997514

Serial Number	Scan Mode	Area*(da) (cm ²)	Isc (mA)	Voc (V)	Pmax (mW)	FF (%)	Eff (%)
39-2#	Isc to Voc	0.0905	2.32	1.128	2.23	85.23	24.66
	Voc to Isc	0.0905	2.32	1.121	2.23	85.46	24.59

Supplementary information: *(da), Designated illumination area

Test results listed in this measurement report refer exclusively to the mentioned test sample.

The results apply only at the time of the test, and do not imply future performance.

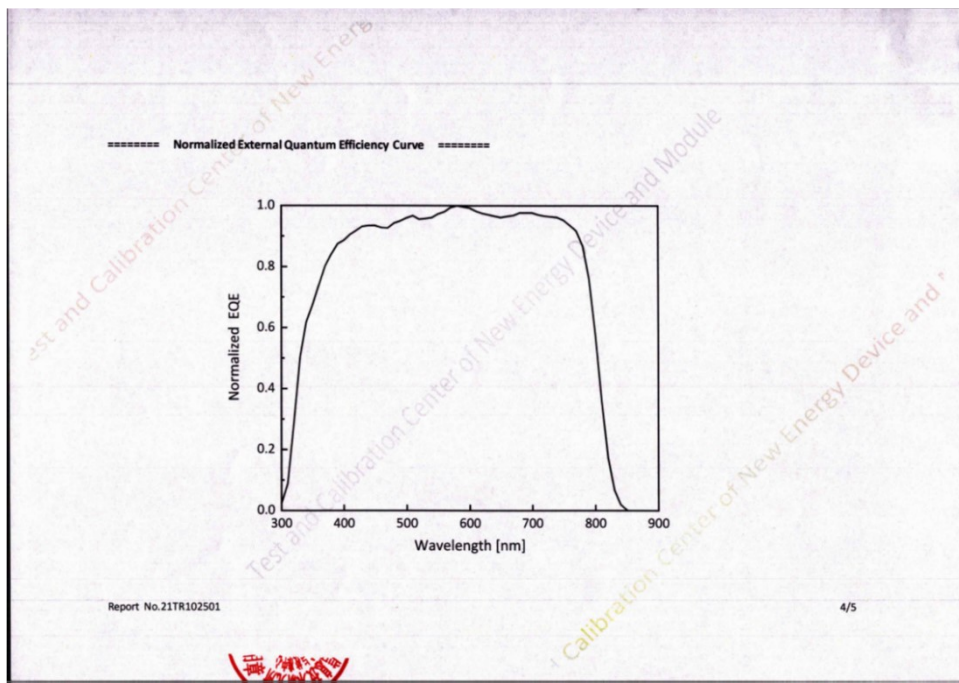
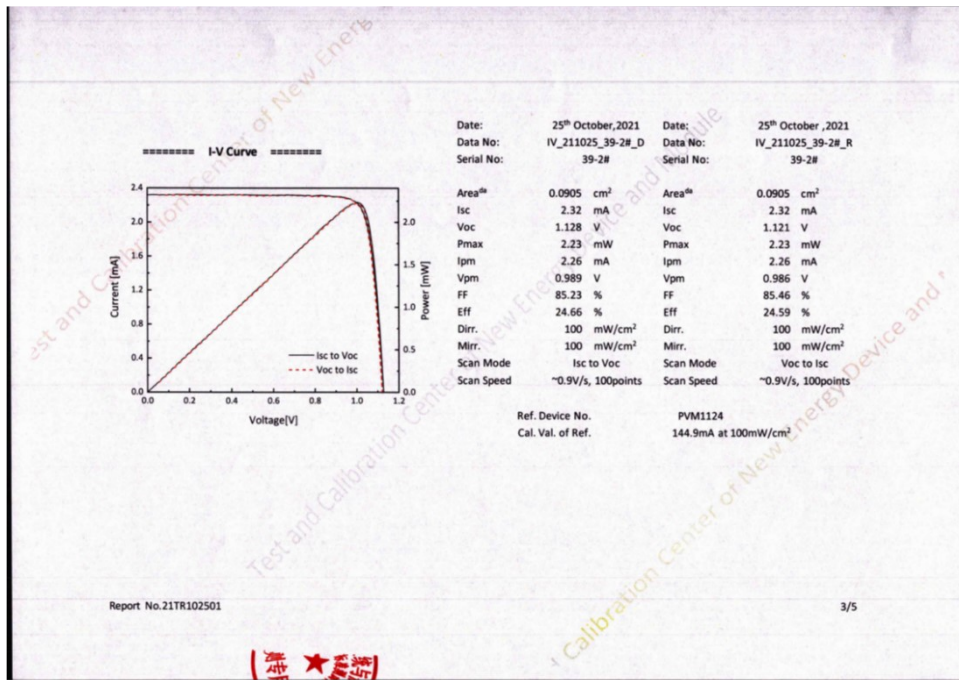


Fig. S6 The certified performance of the target device measured at SIMIT. The device exhibits a certified PCE of 24.66% (under forward scan: $V_{OC} = 1.128$ V, $J_{SC} = 25.64$ mA cm⁻², FF = 85.23%) and 24.59% (under reverse scan: $V_{OC} = 1.121$ V, $J_{SC} = 25.67$ mA cm⁻², FF = 85.46%) with negligible hysteresis.

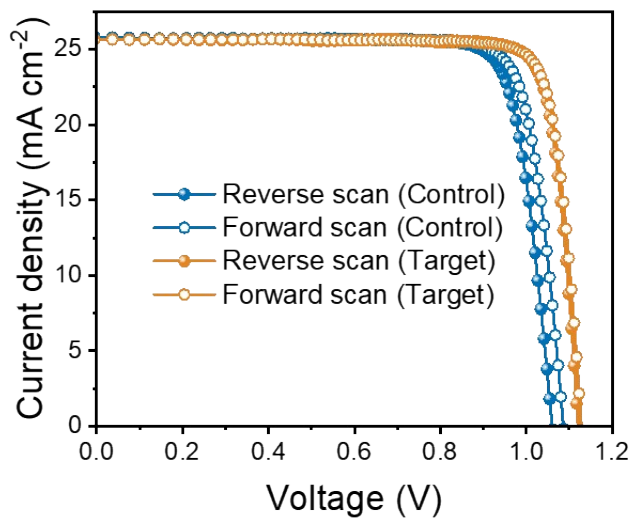


Fig. S7 J - V curves in reverse and forward scans of the control and target devices.

Table S3 Detailed photovoltaic parameters of the J - V curves in reverse and forward scans for the control and target devices.

Devices	Scan direction	V_{OC} (V)	J_{SC} (mA cm ⁻²)	FF (%)	PCE (%)	HI ^a (%)
Control	Reverse	1.060	25.78	82.44	22.53	-2.5
	Forward	1.086	25.76	82.53	23.09	
Target	Reverse	1.121	25.67	85.46	24.59	-0.3
	Forward	1.128	25.64	85.23	24.66	

^a HI: hysteresis index. $HI = (PCE_{Reverse} - PCE_{Forward})/PCE_{Reverse}$

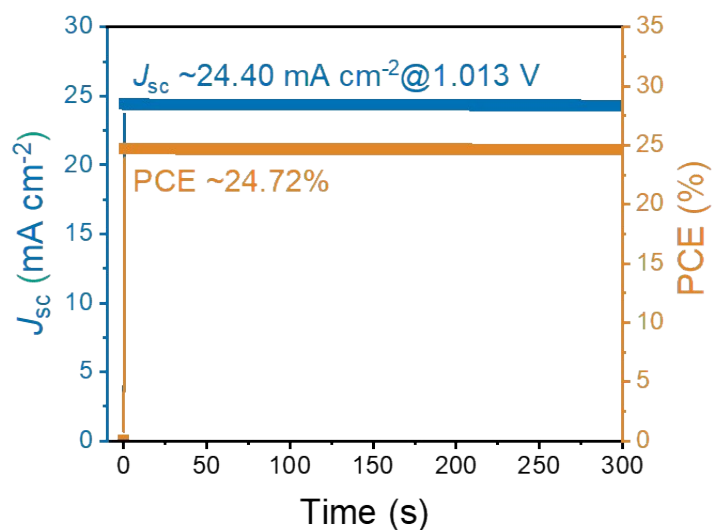


Fig. S8 The stabilized photocurrent and power output of the target device measured at the maximum power point.

S3. Comparison of FF and PCE obtained in this work with those reported in literatures.

Table S4 Comparison of FF and PCE of devices obtained in this work with those reported in literatures with PCE exceeding 24.5%.

Device structure	V _{oc} (V)	J _{sc} (mA cm ⁻²)	FF (%)	PCE (%)	Ref.
FTO/c-TiO ₂ /mp-TiO ₂ /FAPbI ₃ /spiro-mF/Au	1.164	26.35	80.9	24.82	S1
FTO/c-TiO ₂ /mp-TiO ₂ /FA _{0.95} MA _{0.05} PbI ₃ /spiro-OMeTAD/Au	1.189	26.35	81.7	25.59	S2
FTO/c-TiO ₂ /mp-TiO ₂ /FAPbI ₃ :3.8mol% MDACl ₂ /spiro-OMeTAD/Au	1.14	26.5	81.77	24.66	S3
FTO/c-TiO ₂ /mp-TiO ₂ / (FAPbI ₃) _{0.97} (MDA _{0.5} Cs _{0.5}) _{0.03} /spiro-OMeTAD/Au	1.168	26.23	82.15	25.17	S4
ITO/PTAA/Cs _{0.05} (FA _{0.98} MA _{0.02}) _{0.95} Pb(I _{0.98} Br _{0.02}) ₃ /F cTc ₂ /C ₆₀ /BCP/Ag	1.184	25.68	82.32	25.0%	S5
FTO/c-TiO ₂ /mp-TiO ₂ /FAPbI ₃ /Spiro-OMeTAD/Au	1.150	25.86	82.37	24.50	S6
FTO/c-TiO ₂ /mp-TiO ₂ /FAPbI ₃ /spiro-OMeTAD/Au	1.171	26.17	82.47	25.28	S7
FTO/SnO ₂ / FA _x MA _{1-x} PbI _{3-z} Br _z /spiro-MeOTAD/Ag	1.176	25.62	83.15	25.05	S8
FTO/SnO ₂ /FAPbI ₃ :3.8mol% MDACl ₂ /spiro-OMeTAD/Au	1.189	25.74	83.2	25.5	S9
FTO/SnO ₂ /FA _{0.95} Cs _{0.05} PbI ₃ /spiro-OMeTAD/Au	1.144	26.14	83.5	24.98	S10
FTO/SnO ₂ /(FAPbI ₃) _{0.95} (MAPbBr ₃) _{0.05} /P3HT/Au	1.15	25.5	83.8	24.6	S11
FTO/c-TiO ₂ /mp-TiO ₂ /QD-SnO ₂ /FAPbI ₃ /Spiro-OMeTAD/Au	1.176	26.09	83.84	25.72	S12
FTO/SnO ₂ /(FAPbI ₃) _{0.95} (MAPbBr ₃) _{0.05} /(BA) ₂ PbI ₄ /spiro-OMeTAD/Au	1.183	24.67	84.22	24.63	S13
FTO/SnO ₂ /FA _{0.97} MA _{0.03} PbI _{2.91} Br _{0.09} /spiro-OMeTAD/Au	1.158	25.25	84.3	24.7	S14
ITO/SnO ₂ /FA _x MA _{1-x} PbI _{3-z} Br _z /spiro-OMeTAD/Au	1.195	24.9	84.3	25.1	S15
FTO/SnO ₂ /FAPbI ₃ :0.8mol% MAPbBr ₃ /spiro-OMeTAD/Au	1.194	25.09	84.7	25.4	S16
FTO/SnO ₂ /FAPbI ₃ :1.0mol% CsPbBr ₃ /spiro-OMeTAD/Au	1.123	25.72	86.90	25.09	This work

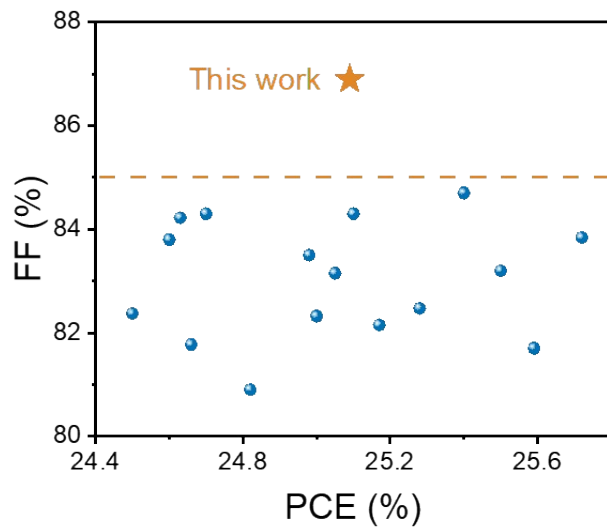


Fig. S9 Comparison of FF and PCE of devices obtained in this work with those reported in literatures with PCE exceeding 24.5% listed in Table S4. Note that FF values reported in these literatures are all smaller than 85%.

Table S5 Detailed parameters of GaAs and perovskite solar cells plotted in Fig. 1e.

	V _{oc} (V)	J _{SC} (mA cm ⁻²)	FF (%)	FF/FF ^{SQ}	PCE (%)	Ref.
GaAs	1.1272	29.78	86.7	96.9%	29.1	S17
Perovskite	1.189	26.35	81.7	90.6%	25.59	S2
	1.184	25.68	82.32	91.2%	25.0%	S5
	1.168	26.23	82.15	91.5%	25.17	S4
	1.171	26.17	82.47	91.7%	25.28	S7
	1.176	25.62	83.15	92.1%	25.05	S8
	1.189	25.74	83.2	92.7%	25.5	S9
	1.176	26.09	83.84	93.0%	25.72	S12
	1.195	24.9	84.3	93.5%	25.1	S15
	1.194	25.09	84.7	93.8%	25.4	S16
	1.123	25.72	86.9	96.3%	25.09	This work

S4. Stability data.

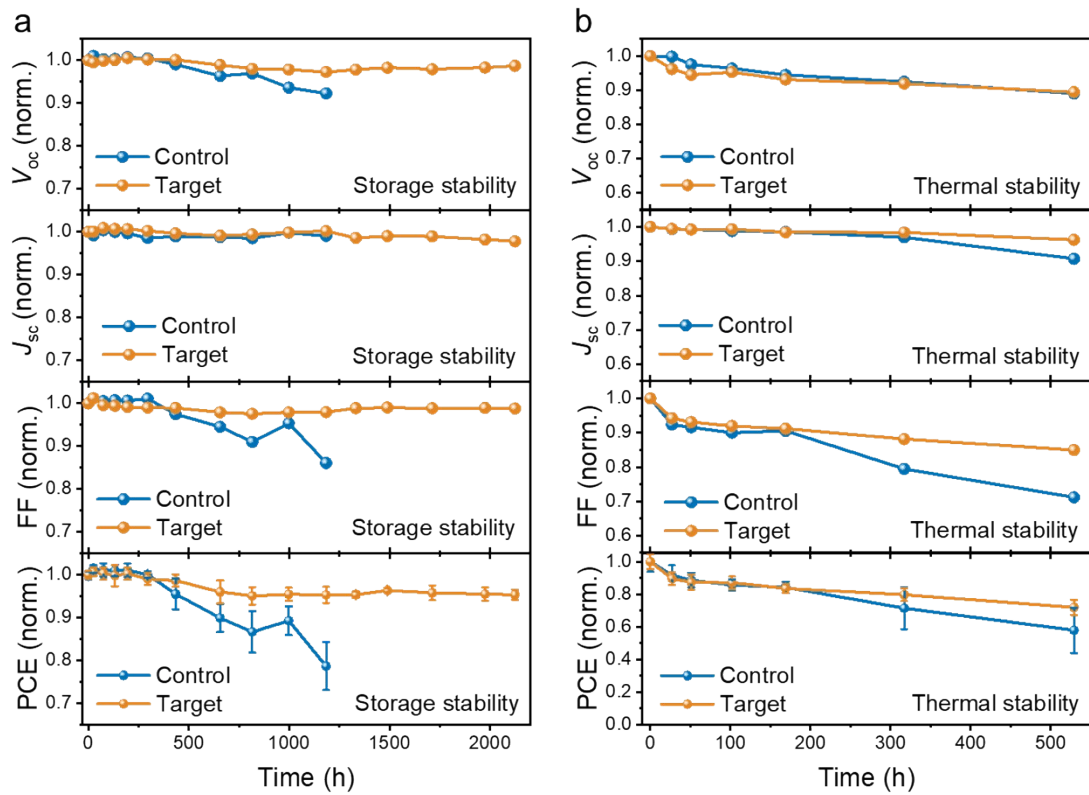


Fig. S10 **a** Normalized V_{oc} , J_{sc} , FF and PCE of the control and target devices evolve with the storage time (stored in a dry box at room temperature and 15% relative humidity). **b** Normalized V_{oc} , J_{sc} , FF and PCE of the control and target devices evolve with the heating time (heated at 85°C in N₂ glovebox). PTAA was used to replace spiro-OMeTAD as the hole transport layer for the thermal stability measurement.

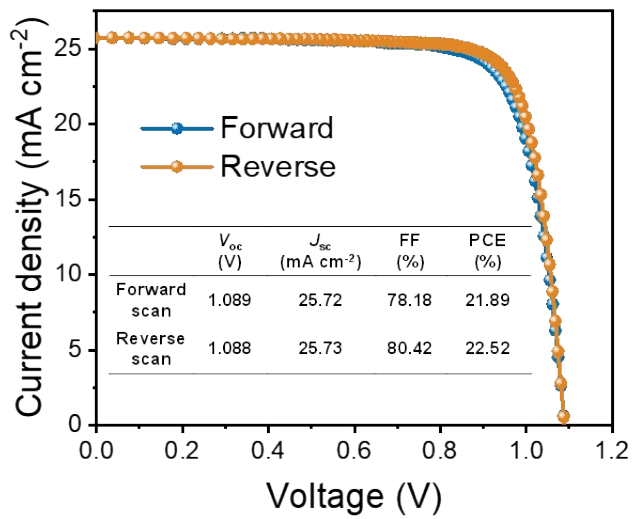


Fig. S11 J - V curves for the best-performing target devices based on PTAA HTL measured by forward and reverse scans.

S5. XRD patterns of FAPbI₃ films with different amounts of CsPbBr₃.

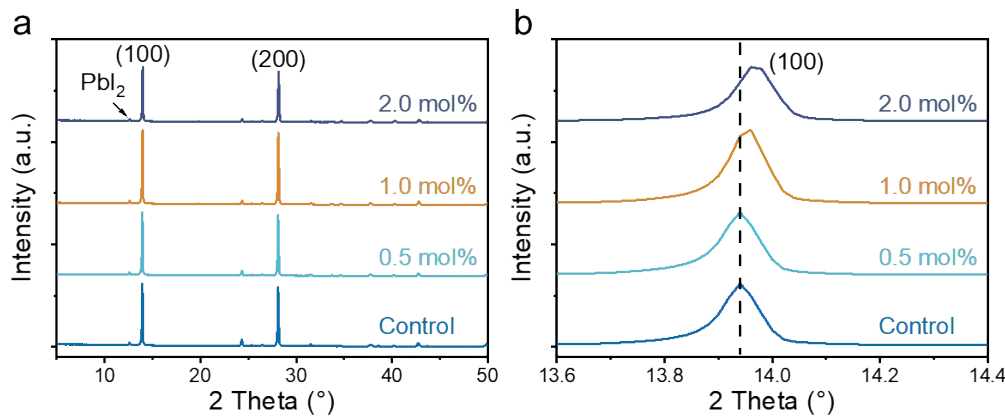


Fig. S12 **a** XRD patterns of FAPbI₃ films with different amounts of CsPbBr₃ annealed at 120 °C for 1 hour. **b** Enlarged region between 13.6° and 14.4° in (a).

Table S6 The diffraction parameters extracted from the XRD patterns of five samples

in each case.

xCsPbBr ₃ -FAPbI ₃	2 Theta at (100)	FWHM at (100)
0%	13.959°±0.003°	0.102°±0.001°
0.5%	13.966°±0.007°	0.090°±0.002°
1.0%	13.977°±0.001°	0.086°±0.001°
2.0%	13.986°±0.006°	0.089°±0.003°

^a FWHM: full width at half maximum.

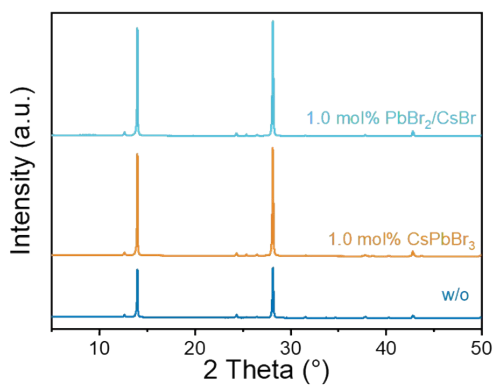


Fig. S13 XRD patterns of FAPbI₃ films without and with pre-crystallized CsPbBr₃ and PbBr₂/CsBr powder.

Table S7 The diffraction parameters extracted from the XRD patterns (Fig. S13).

Additive	2 Theta at (100)	FWHM at (100)
w/o	13.957°	0.103°
1.0 mol% CsPbBr ₃	13.973°	0.090°
1.0 mol% PbBr ₂ /CsBr	13.973°	0.092°

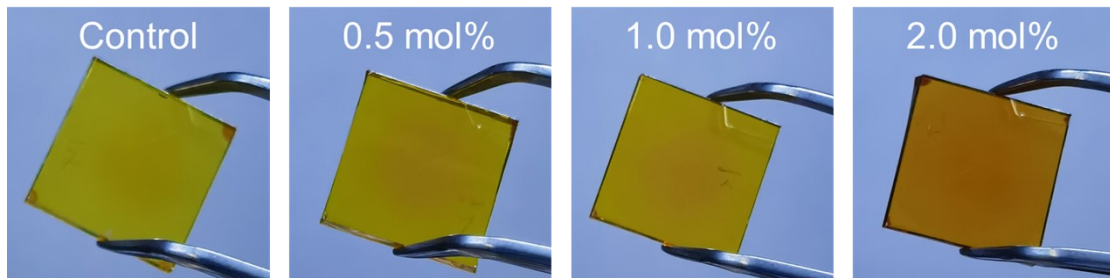


Fig. S14 Photographs of FAPbI₃ films with different amounts of CsPbBr₃ additives immediately after anti-solvent treatment without any thermal annealing.

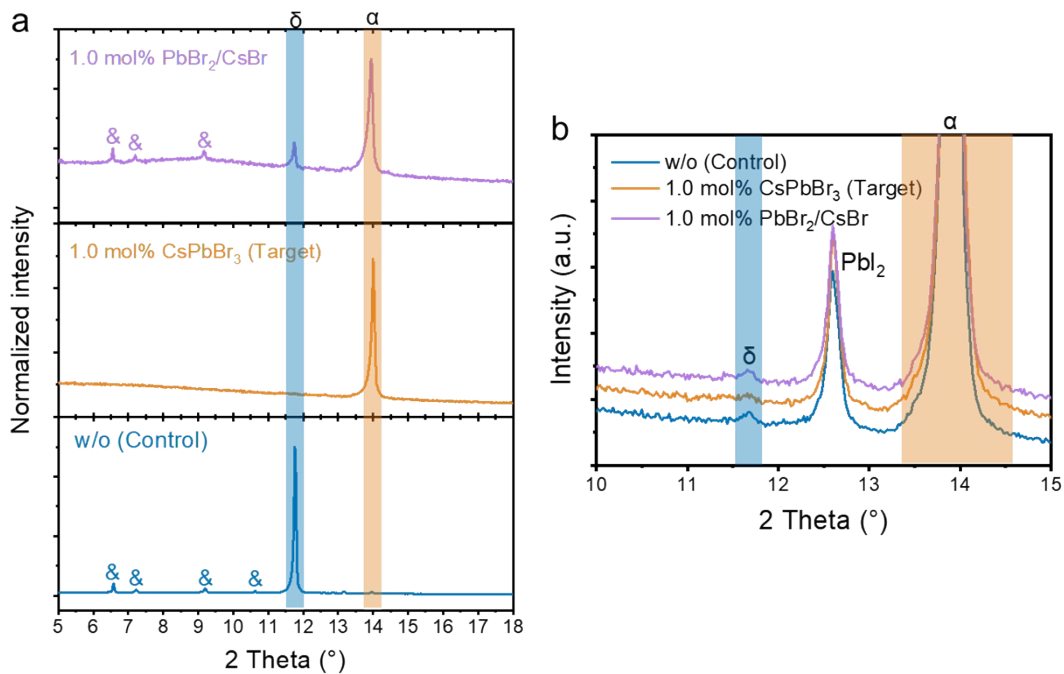


Fig. S15 a XRD patterns of FAPbI₃ (control), 1.0 mol% CsPbBr₃-FAPbI₃ (target) and 1.0 mol% PbBr₂/CsBr-FAPbI₃ immediately after anti-solvent treatment without any thermal annealing. **b** XRD patterns of FAPbI₃ (control), 1.0 mol% CsPbBr₃-FAPbI₃ (target) and 1.0 mol% PbBr₂/CsBr-FAPbI₃ annealed at 120 °C for 1 hour.

S6. Geometric illustration of the crystal structure and radially integrated curves extracted from GIXRD patterns.

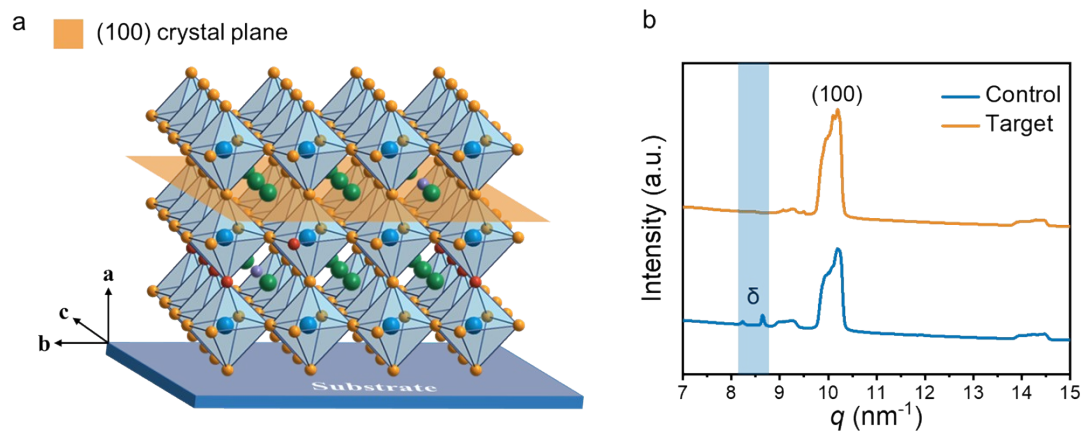


Fig. S16 **a** Geometric illustration of the crystal structure and preferred orientation of perovskite film. **b** Radially integrated curves of FAPbI_3 (control) and 1.0 mol% $\text{CsPbBr}_3\text{-FAPbI}_3$ (target).

S7. SEM images of FAPbI₃ and 1.0 mol% CsPbBr₃-FAPbI₃ perovskite films.

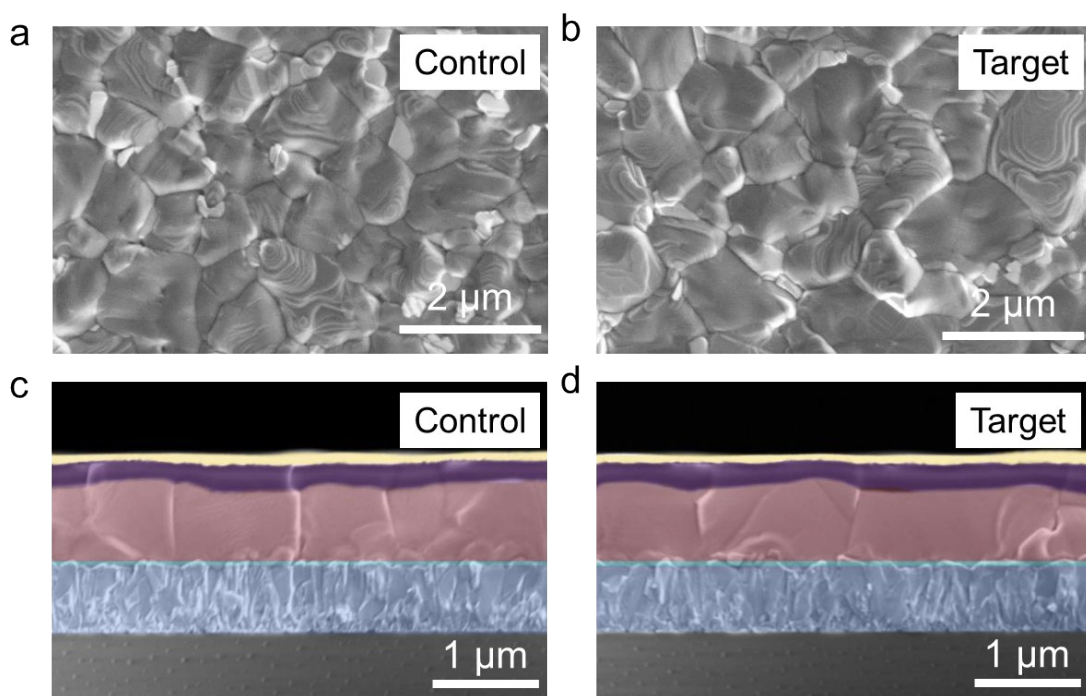


Fig. S17 **a, b** Top surface SEM images of FAPbI₃ (control) and 1.0 mol% CsPbBr₃-FAPbI₃ (target). **c, d** Cross-sectional SEM images of FAPbI₃ (control) and 1.0 mol% CsPbBr₃-FAPbI₃ (target).

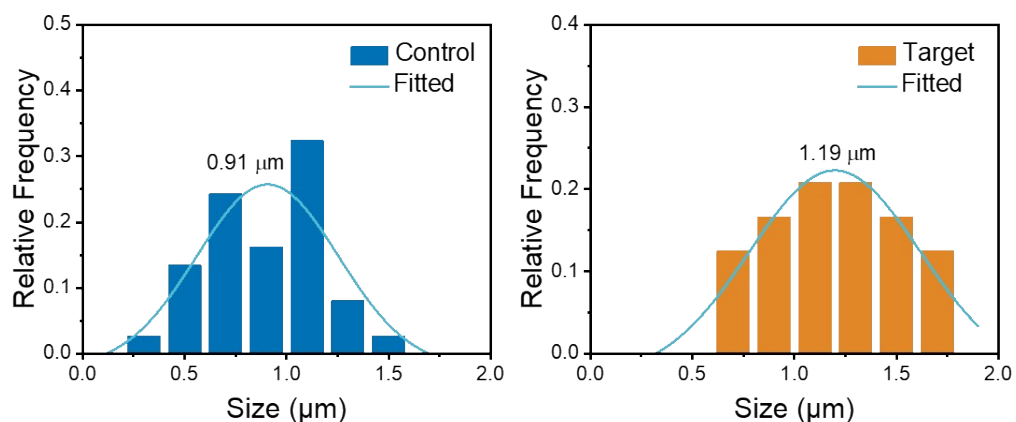


Fig. S18 The statistic distribution of grain sizes extracted from the Fig. S17a and b.

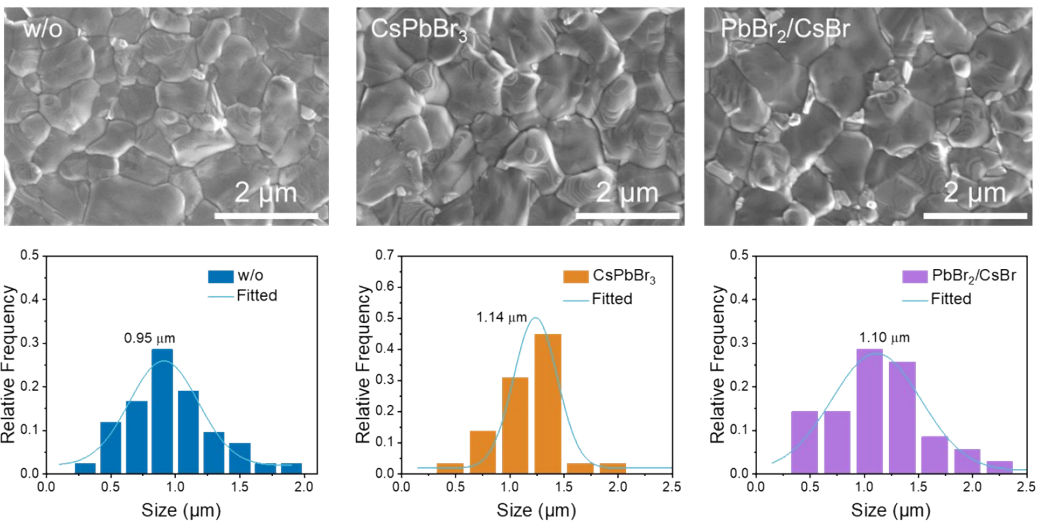


Fig. S19 Top surface SEM images and statistic distribution of grain sizes of FAPbI₃ without and with pre-crystallized CsPbBr₃ and PbBr₂/CsBr powder, respectively.

S8. TAS at different delay times.

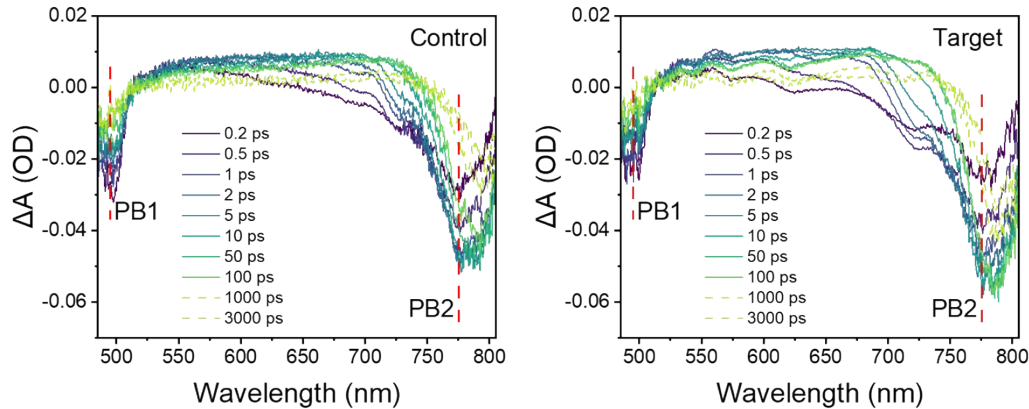


Fig. S20 TAS of FAPbI₃ (control) and 1.0 mol% CsPbBr₃-FAPbI₃ (target) films excited at 400 nm.

Table S8 Transient absorption fitted kinetics parameters for glass/FAPbI₃ (control) and glass/1.0 mol% CsPbBr₃-FAPbI₃ (target) films at 775 nm.

	A ₁	τ ₁ (ps)	A ₂	τ ₂ (ps)	τ _{ave} (ps)
Control	0.59	286	0.41	3260	2926
Target	0.57	423	0.43	6815	6329

The results are fitted with the following double exponential equation:^{S18}

$$y = y_0 + A_1 \exp\left(-\frac{t}{\tau_1}\right) + A_2 \exp\left(-\frac{t}{\tau_2}\right)$$

The average decay time is calculated through the following format:

$$\tau_{ave} = \frac{A_1 \tau_1^2 + A_2 \tau_2^2}{A_1 \tau_1 + A_2 \tau_2}$$

S9. UV-vis spectra and the plots of $(\alpha h\nu)^2$ vs energy ($h\nu$) of the control and target perovskite films.

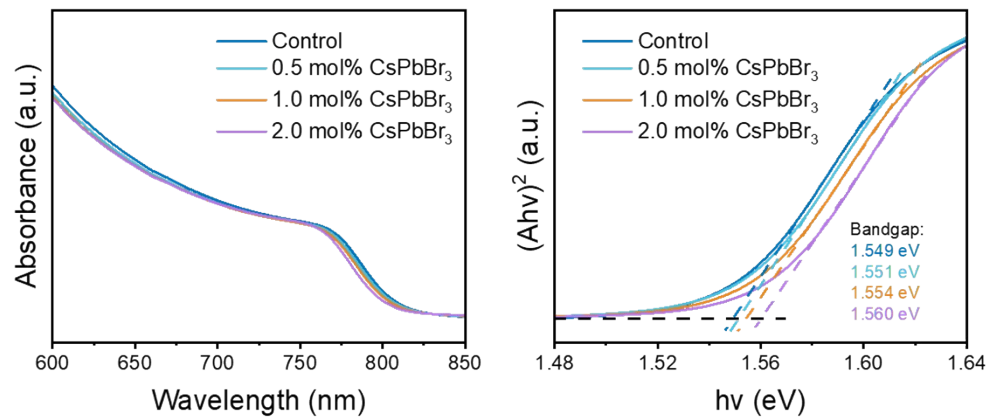


Fig. S21 UV-vis spectra and the plots of $(\alpha h\nu)^2$ vs energy ($h\nu$) of FAPbI₃ (control) without and with different amount of CsPbBr₃ incorporation.

S10. Enlarged DLTS spectra and Arrhenius plot.

DLTS uses the transient capacitance of p-n junction at different temperature as a probe to monitor the changes in charge state of a deep defect center. Traps in the device are filled by carriers through applying a voltage pulse to the device, which changes the capacitance associated with p-n junction of the device. The types of traps can be differentiated by the change of capacitance during the discharging process of traps (the hole and electron traps correspond to negative and positive ΔC , respectively in n type films). The defect level is identified from DLTS signal using Fourier deconvolution algorithm, and Arrhenius plots are obtained from defect peaks in DLTS signal. The active energy (E_a , E_C-E_T or E_T-E_V) and capture cross section of electron traps and hole traps can be calculated by the Arrhenius equations S1 and S2,^{S19,20}

$$\ln(\tau_e v_{th,n} N_C) = \frac{E_C - E_T}{k_B T} - \ln(X_n \sigma_n) \quad (S1)$$

$$\ln(\tau_e v_{th,p} N_V) = \frac{E_T - E_V}{k_B T} - \ln(X_p \sigma_p) \quad (S2)$$

where τ_e , N_C , N_V , E_C , E_T and E_V are emission time constant, conduction band state density, valence band state density, conduction band, trap energy level and valence band, respectively. $v_{th,n/p}$, $X_{n/p}$ and $\sigma_{n/p}$ represent thermal velocity, entropy factor and capture cross section for electron and hole, respectively. The E_a and σ can be extracted by the slope and y-axis intercept, separately. In addition, the trap density (N_T) could be obtained by equation S3,^{S19}

$$N_T = 2N_S \frac{\Delta C}{C_R} \quad (S3)$$

where N_S is the shallow donor concentration, C_R is the capacitance under reverse bias,

while ΔC represents the amplitude of transient capacitance.

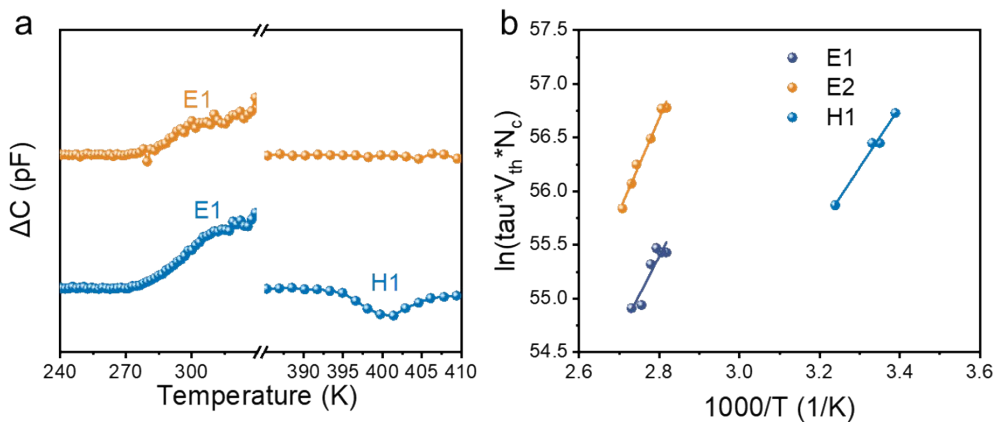


Fig. S22 **a** Enlarged DLTS spectra of the control and target devices in Fig. 3c. **b** Arrhenius plot of control device to determine energy and capture cross section.

Table S9 The defect parameters of control and target devices.

Defects	$E_C - E_T^a$ (eV)	σ^b (cm^2)	N_T^c (cm^{-3})	N_S^d (cm^{-3})
Control	E1	0.662	2.263×10^{-15}	1.455×10^{13}
	E2	0.734	2.012×10^{-16}	2.278×10^{14}
	H1	0.832	5.008×10^{-16}	7.781×10^{11}
Target	E1	0.658	3.291×10^{-15}	4.278×10^{12}
	E2	0.732	1.843×10^{-16}	9.871×10^{13}

^a E_T : the energy level of defect; ^b σ : capture cross-sections of traps; ^c N_T : trap concentration. ^d N_S : shallow donor concentration.

S11. SCLC analysis.

Electron-only device with a structure of glass/FTO/SnO₂/perovskite/[6,6]-phenyl-C₆₁-butyric acid methyl ester (PC₆₁BM)/Ag and hole-only device with a structure of ITO/PTAA/perovskite/spiro-OMeTAD/Au was fabricated to determine the trap density within the perovskite films. The corresponding *I*–*V* curves are plotted in Fig. 2g and 2h. The linear correlation of *I*–*V* characteristics at low bias voltage suggesting an ohmic response. When the bias voltage exceeds the kink point, the current increases nonlinearly, representing where the trap-states are filled completely, the corresponding bias voltage at the kink point is defined as the trap-filled limit voltage (*V*_{TFL}), and the trap-state density (*n*_t) can be determined through Equation S4:

$$n_t = \frac{2\epsilon_0\epsilon_r}{qL^2} \cdot V_{TFL} \quad (\text{S4})$$

Where ϵ_0 is the vacuum permittivity, ϵ_r is the relative dielectric constant of perovskite ($\epsilon_r = 46.9$),^{S21} q is the elementary charge of the electron, and L is the perovskite film thickness (about 750 nm estimated from the cross-sectional SEM images). V_{TFL} is the onset voltage of the trap-filled limit region.

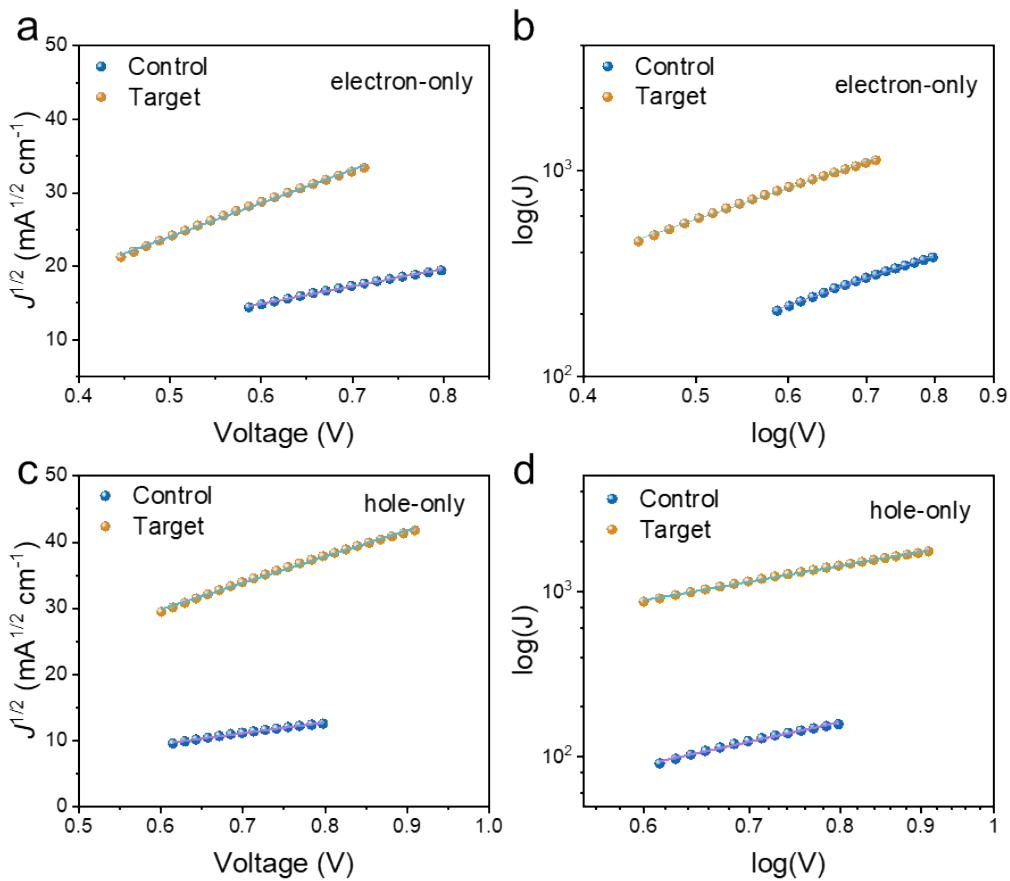


Fig. S23 J - V curves of the electron-only devices (a) (FTO/SnO₂/perovskite/PC₆₁BM/Ag) and hole-only devices (c) (ITO/PTAA/perovskite/spiro-OMeTAD/Au) in SCLC region. The log(J)-log(V) plots of the devices in the SCLC region with a slope of 2 for the electron-only devices (b) and hole-only devices (d), respectively. The solid lines are fits of the data points.

Table S10 The charge carrier mobilities obtained from the electron-only and hole-only devices.

Device	Mobility (10 ⁻³ cm ² V ⁻¹ s ⁻¹)		μ_e/μ_h
	Electron	Hole	
Control	5.1	2.4	2.1
Target	18.7	14.3	1.3

The carrier mobilities are obtained according to the SCLC regions, the dark current is fitted by Mott-Gurney law:

$$J = \frac{9\epsilon\epsilon_0\mu}{8L^3}V^2 \quad (\text{S5})$$

Where the J is current density and μ is carrier mobility. According to equation S5, the calculated μ_h are 2.4×10^{-3} and $14.3 \times 10^{-3} \text{ cm}^2 \text{ V}^{-1} \text{ s}^{-1}$ for control and target perovskite films, respectively. And the calculated μ_e are 5.1×10^{-3} and $18.7 \times 10^{-3} \text{ cm}^2 \text{ V}^{-1} \text{ s}^{-1}$ for control and target perovskite films, respectively.

S12. EIS analysis.

From the Nyquist plot (Fig. S24), the impedance spectra were fitted with one R-CPE arcs, which a resistor R_s (series resistance) connects with an R-CPE elements. R_s is determined by the starting point at the real part of the Nyquist plot. The R_{ct} (charge transport resistance) is related to the charge transfer dynamics of devices, CPE is the non-ideal chemical capacitances. According to the fitting data in Table S11, after CsPbBr_3 incorporating the R_s value decreases from 14.21 to 11.31 Ω , and R_{ct} value also decreases from 380.7 to 276.7 Ω .

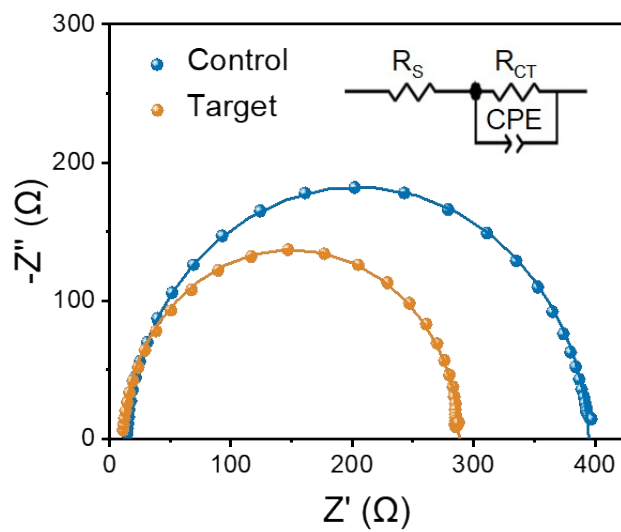


Fig. S24 Nyquist plots of the control and target devices. Inset: the equivalent circuit model employed for the fitting of the impedance spectra.

Table S11 Parameters employed for the fitting of the impedance spectra of control and target devices.

Device	R_s (Ω)	R_{ct} (Ω)	CPE-T (F)	CPE-P (F)
Control	14.21	380.7	1.22E-8	0.97
Target	11.31	276.7	1.15E-8	0.99

S13. Dark J - V curves of the control and target devices.

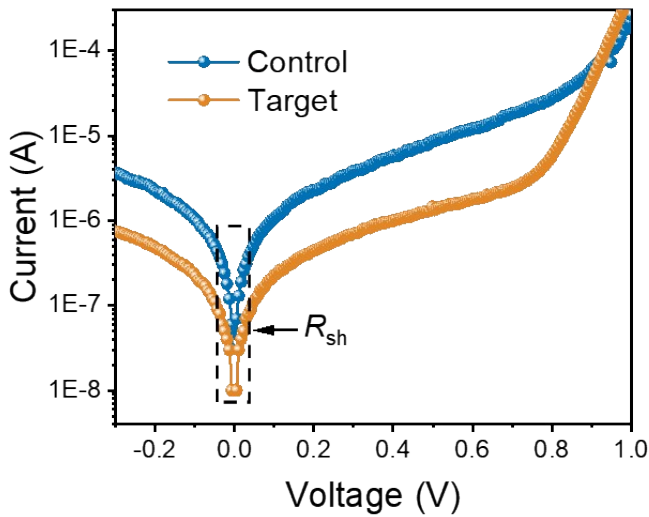


Fig. S25 Dark J - V curves of the control and target devices.

S14. FF loss analysis.

Recombination currents and ohmic resistances have a deep influence on the FF of solar cells. To account for these effects, the two-diode model of solar cells, which includes two diodes with saturation current densities J_{01} , J_{02} and ohmic resistors R_s , R_{sh} in series and parallel to the diodes, is usually used.^{S22}

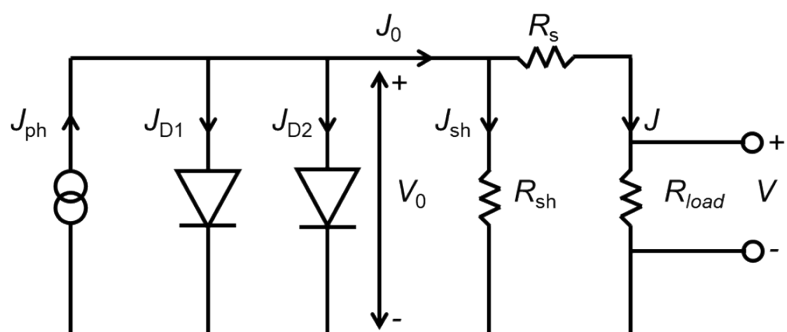


Fig. S26 Schematic of the two-diode model of a solar cell.

A practical upper limit of fill factor (FF_{J01}) is determined by assuming the absence of R_s , R_{sh} and J_{02} .

$$J = J_{ph} - J_{01} \left[\exp \left(\frac{qV}{k_B T} \right) - 1 \right] \quad (S6)$$

At open-circuit condition, $J = 0$ and $V = V_{oc}$. At short-circuit condition, $J = J_{sc}$, $V = 0$.

The equation S6 could be converted into equation S7.

$$J = J_{sc} - \frac{J_{sc}}{\exp \left(\frac{qV_{oc}}{k_B T} \right) - 1} \left[\exp \left(\frac{qV}{k_B T} \right) - 1 \right] \quad (S7)$$

$$FF_{J01} = \frac{J_{01}V_{01}}{J_{sc}V_{oc}} \quad (S8)$$

According to the above equations, the calculated FF_{J01} are 89.0% and 89.2% for control and target devices.

Considering the two-diode model at MPP, the terminal voltage and current density will be related to R_s and R_{sh} .

$$V_{mpp} = V_0 - J_{mpp}R_s \quad (S9)$$

$$J_{mpp} = J_0 - (V_{mpp} + J_{mpp}R_s)/R_{sh} \quad (S10)$$

Thus,

$$\frac{V_0J_0}{V_{oc}J_{sc}} = \frac{V_{mpp}J_{mpp}}{V_{oc}J_{sc}} + \frac{J_{mpp}^2 R_s}{V_{oc}J_{sc}} + \frac{(V_{mpp} + J_{mpp}R_s)^2}{R_{sh}V_{oc}J_{sc}} \quad (S11)$$

where $\frac{V_{mpp}J_{mpp}}{V_{oc}J_{sc}}$ is the FF. $\frac{J_{mpp}^2 R_s}{V_{oc}J_{sc}}$ is the ΔFF_{Rs} and $\frac{(V_{mpp} + J_{mpp}R_s)^2}{R_{sh}V_{oc}J_{sc}}$ is the ΔFF_{Rsh} .

The FF loss due to J_{02} recombination can be obtained according to the following equation S12.

$$\Delta FF_{J02 \text{ recombination}} = FF_{J01} - \Delta FF_{Rs} - \Delta FF_{Rsh} - FF \quad (S12)$$

R_s and R_{sh} need to be measured to calculate the ΔFF_{Rs} and ΔFF_{Rsh} . After that, three terms of FF loss could be obtained.

R_s at MPP was determined from the voltage shift at J_{mpp} between the one sun $J-V$ curve and pseudo $J-V$ curve (Fig. 4e). Pseudo $J-V$ curves were obtained by measuring the $J-V$ curve at different light intensities and then converting the J_{sc} - V_{oc} pairs into pseudo $J-V$ curves using Equation S13,^{S23}

$$J(V_{oc}) = J_{sc}^{one\ sun}[1 - \frac{J_{sc}^{filtered}(V_{oc})}{J_{sc}^{one\ sun}}] \quad (S13)$$

R_{sh} was determined by the inverse of the slope of a linear fit of the dark $J-V$ in the range 0-50 mV (Fig. S25).

The corresponding values are summarized in Table S12.

Table S12 The one sun $J-V$ data and FF analysis results.

Device	V_{oc} (V)	J_{sc} (mA cm^{-2})	FF (%)	PCE (%)	V_{mpp} (V)	J_{mpp} (mA cm^{-2})
Control	1.087	25.75	83.47	23.37	0.952	24.54
Target	1.123	25.72	86.90	25.09	1.014	24.75
Device	R_s at MPP ($\Omega \text{ cm}^2$)	R_{sh} ($\Omega \text{ cm}^2$)	FF _{J01} (%)	ΔFF_{Rs}	ΔFF_{Rsh}	ΔFF_{J02}
					(% absolute)	
Control	1.2	2.8×10^3	89.0	2.58	1.23	1.72
Target	0.6	6.2×10^3	89.2	1.27	0.59	0.58

References

- S1. M. Jeong, I. W. Choi, E. M. Go, Y. Cho, M. Kim, B. Lee, S. Jeong, Y. Jo, H. W. Choi, J. Lee, J.-H. Bae, S. K. Kwak, D. S. Kim and C. Yang, *Science*, 2020, **369**, 1615-1620.
- S2. J. Jeong, M. Kim, J. Seo, H. Lu, P. Ahlawat, A. Mishra, Y. Yang, M. A. Hope, F. T. Eickemeyer, M. Kim, Y. J. Yoon, I. W. Choi, B. P. Darwich, S. J. Choi, Y. Jo, J. H. Lee, B. Walker, S. M. Zakeeruddin, L. Emsley, U. Rothlisberger, A. Hagfeldt, D. S. Kim, M. Grätzel and J. Y. Kim, *Nature*, 2021, **592**, 381-385.
- S3. H. Min, M. Kim, S.-U. Lee, H. Kim, G. Kim, K. Choi, J. H. Lee and S. I. Seok, *Science*, 2019, **366**, 749-753.
- S4. G. Kim, H. Min, K. S. Lee, D. Y. Lee, S. M. Yoon and S. I. Seok, *Science*, 2020, **370**, 108-112.
- S5. Z. Li, B. Li, X. Wu, S. A. Sheppard, S. F. Zhang, D. P. Gao, N. J. Long and Z. L. Zhu, *Science*, 2022, **376**, 416-420.
- S6. L. Zhao, Q. Li, C. H. Hou, S. Li, X. Yang, J. Wu, S. Zhang, Q. Hu, Y. Wang, Y. Zhang, Y. Jiang, S. Jia, J. J. Shyue, T. P. Russell, Q. Gong, X. Hu and R. Zhu, *J. Am. Chem. Soc.*, 2022, **144**, 1700-1708.
- S7. M. Kim, I.-w. Choi, S. J. Choi, J. W. Song, S.-I. Mo, J.-H. An, Y. Jo, S. Ahn, S. K. Ahn, G.-H. Kim and D. S. Kim, *Joule*, 2021, **5**, 659-672.
- S8. X. Luo, Z. Shen, Y. Shen, Z. Su, X. Gao, Y. Wang, Q. Han and L. Han, *Adv. Mater.*, 2022, DOI: 10.1002/adma.202202100, 2202100.
- S9. H. Min, D. Y. Lee, J. Kim, G. Kim, K. S. Lee, J. Kim, M. J. Paik, Y. K. Kim, K. S. Kim, M. G. Kim, T. J. Shin and S. I. Seok, *Nature*, 2021, **598**, 444-450.
- S10. S.-H. Lee, S. Jeong, S. Seo, H. Shin, C. Ma and N.-G. Park, *ACS Energy Lett.*, 2021, **6**, 1612-1621.
- S11. M. J. Jeong, K. M. Yeom, S. J. Kim, E. H. Jung and J. H. Noh, *Energy Environ. Sci.*, 2021, **14**, 2419-2428.
- S12. M. Kim, J. Jeong, H. Lu, T. K. Lee, F. T. Eickemeyer, Y. Liu, I. W. Choi, S. J. Choi, Y. Jo, H.-B. Kim, S.-I. Mo, Y.-K. Kim, H. Lee, N. G. An, S. Cho, W. R. Tress, S. M. Zakeeruddin, A. Hagfeldt, J. Y. Kim, M. Grätzel and D. S. Kim, *Science*, 2022, **375**, 302-306.
- S13. Y.-W. Jang, S. Lee, K. M. Yeom, K. Jeong, K. Choi, M. Choi and J. H. Noh, *Nat. Energy*, 2021, **6**, 63-71.
- S14. F. Zhang, S. Y. Park, C. Yao, H. Lu, S. P. Dunfield, C. Xiao, S. Uličná, X. Zhao, L. D. Hill, X. Chen, X. Wang, L. E. Mundt, K. H. Stone, L. T. Schelhas, G. Teeter, S. Parkin, E. L. Ratcliff, Y.-L. Loo, J. J. Berry, M. C. Beard, Y. Yan, B. W. Larson and K. Zhu, *Science*, 2022, **375**, 71-76.
- S15. Z. Shen, Q. Han, X. Luo, Y. Shen, T. Wang, C. Zhang, Y. Wang, H. Chen, X. Yang, Y. Zhang and L. Han, *Energy Environ. Sci.*, 2022, **15**, 1078-1085.
- S16. J. J. Yoo, G. Seo, M. R. Chua, T. G. Park, Y. Lu, F. Rotermund, Y. K. Kim, C. S. Moon, N. J. Jeon, J. P. Correa-Baena, V. Bulovic, S. S. Shin, M. G. Bawendi and J. Seo, *Nature*, 2021, **590**, 587-593.

-
- S17. M. A. Green, E. D. Dunlop, J. Hohl - Ebinger, M. Yoshita, N. Kopidakis and X. Hao, *Prog. Photovoltaics*, 2021, **30**, 3-12.
 - S18. J. Zhang, L. Wang, C. Jiang, B. Cheng, T. Chen and J. Yu, *Adv. Sci.*, 2021, **8**, 2102648.
 - S19. W. Lian, C. Jiang, Y. Yin, R. Tang, G. Li, L. Zhang, B. Che and T. Chen, *Nat. Commun.*, 2021, **12**, 3260.
 - S20. W. P. Hu, X. He, Z. M. Fang, W. T. Lian, Y. B. Shang, X. C. Li, W. R. Zhou, M. M. Zhang, T. Chen, Y. L. Lu, L. J. Zhang, L. M. Ding and S. F. Yang, *Nano Energy*, 2020, **68**, 104362.
 - S21. W. Hu, W. Zhou, X. Lei, P. Zhou, M. Zhang, T. Chen, H. Zeng, J. Zhu, S. Dai, S. Yang and S. Yang, *Adv. Mater.*, 2019, **31**, 1806095.
 - S22. A. Khanna, T. Mueller, R. A. Stangl, B. Hoex, P. K. Basu and A. G. Aberle, *IEEE J. Photovolt.*, 2013, **3**, 1170-1177.
 - S23. N. Mundhaas, Z. S. J. Yu, K. A. Bush, H. P. Wang, J. Hausele, S. Kavadiya, M. D. McGehee and Z. C. Holman, *Sol. RRL*, 2019, **3**, 1800378.